CHEMISTRY OF MATERIALS

pubs.acs.org/cm Article

Doping Effect on the Magnetism of Thiolate-Capped 25-Atom Alloy Nanoclusters

Yingwei Li,[‖ Y.L. and S.B.] Saborni Biswas,[‖ Y.L. and S.B.] Tian-Yi Luo, Rosalba Juarez-Mosqueda, Michael G. Taylor, Giannis Mpourmpakis, Nathaniel L. Rosi, Michael P. Hendrich,* and Rongchao Jin*

Cite This: *Chem. Mater.* 2020, 32, 9238−9244 Read Online

ACCESS | Metrics & More | Article Recommendations | Supporting Information

ABSTRACT: The magnetism of metal nanoclusters (NCs) with discrete electronic structures differs from that of metallic-state nanoparticles. Among the gold NCs, magnetic ones are rare. While 7e $[Au_{25}(SR)_{18}]^0$ (SR = thiolate) was an earlier reported one to be magnetic, its spin properties are yet to be understood. Here, we report the silver-doping effect on the magnetic properties of a series of $[Au_{25-x}Ag_x(SR)_{18}]^0$ with x ranging from 1 to maximum 9 through analysis by electron paramagnetic resonance (EPR) spectroscopy. This series of M_{25} (M = Au/Ag) NCs reveals a linear decrease in axial splitting with increasing Ag doping owing to smaller spin−orbit coupling for Ag in comparison to Au, and X-ray crystallography analysis reveals the sites for Ag doping, which provides a basis for understanding the spin properties. The influence of aromatic vs nonaromatic ligands on the EPR signals has also been compared. The electronic structures of M_{25} NCs have been computed. Overall, this work demonstrates an effective strategy to manipulate the spin properties of NCs by atomically controlled Ag doping.

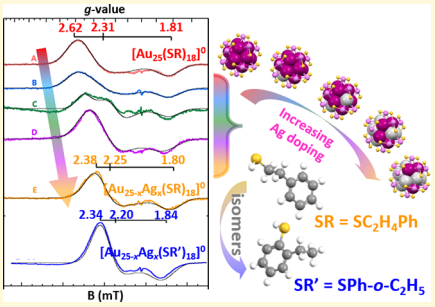

INTRODUCTION

The physical and chemical properties of nanoparticles (NPs) are known to be significantly affected by their size and surface, as both factors greatly affect the particle surface energy, resulting in different electron redistributions (e.g., s−d rehybridization for d-band metals) from surface atoms to inner ones.[1,2] Functional ligands, e.g., thiols (HSR), are effective in stabilizing metal NPs owing to the strong affinity between Au and S, and the strong Au−S bonds also induce a distinct charge transfer, potentially leading to magnetism in Au−SR NPs.[3−7] It was observed that the d-hole population of surface Au atoms increases as the size of Au NPs decreases,[1] making the NPs show magnetic properties. Hori et al. earlier reported low-temperature ferromagnetic spin polarization in Au NPs with the maximum value being achieved at a diameter of ∼3 nm,[8] and Gallani et al. observed ferromagnetic-like and paramagnetic behaviors for 4.4 and 1.9 nm Au NPs, respectively.[9] Fernández et al. further showed room-temperature magnetic hysteresis in 1.4 nm Au−SR NPs.[10] Dodecanethiol-capped Au, Ag, and Cu NPs of ∼2 nm all showed similar characteristics with high magnetic moments.[2] Thus, ultrasmall metal-thiolate NPs are intriguing systems for studying the magnetic properties, in which the factors such as the strong covalency of surface bonds as well as the large proportion of surface atoms generally play important roles.

Although the magnetic properties of Au−SR NPs hold promise in various applications, including magneto-optical data storage, recyclable nanocatalysts, magnetic resonance imaging, etc,[11−13] the magnetic properties of Au NPs are still poorly understood, and there are conflicting results in the literature, especially with respect to magnetic ordering. Given the fact that many of the interesting aspects of Au NPs are thought to come from defects in the structure, the atomically precise nanoclusters (NCs) might shed light on these aspects.

The recently developed metal NCs of atomic precision provide a new opportunity to correlate the structure and properties.[14−16] These NCs of specific compositions with their total structures resolved by X-ray crystallography are in the size range of showing interesting magnetic properties. However, the vast majority of reported M-SR (M = Au, Ag, Cu, Pt, Pd, etc.) NCs are diamagnetic due to valence electron pairing to fulfill the electronic closed-shell configuration,[17] with only a few open-shell cases.[18−23] The paradigm case is the paramagnetic $[Au_{25}(PET)_{18}]^0$, in which the number of valence electrons is counted to be 25−18 = 7e, and the presence of one unpaired electron in the highest occupied molecular orbital (HOMO) is responsible for the observed paramagnetism. The spin is found to be primarily originated from the icosahedral Au_{13} kernel.[18,24] It is worth noting that Roduner et al. reported the intriguing magnetic properties of bare Pt_{13} embedded in the zeolite pores.[17] Many mysteries of the magnetic properties in the cluster state still remain to be deciphered.[25]

Received: July 18, 2020
Revised: October 6, 2020
Published: October 20, 2020

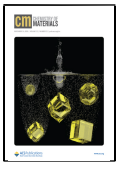

Downloaded via UNIV OF PITTSBURGH on November 11, 2020 at 18:03:17 (UTC).
See https://pubs.acs.org/sharingguidelines for options on how to legitimately share published articles.

ACS Publications © 2020 American Chemical Society

https://dx.doi.org/10.1021/acs.chemmater.0c02984
Chem. Mater. 2020, 32, 9238−9244

Herein, we report the manipulation of the 7e paramagnetic $[Au_{25}(SR)_{18}]^0$ by Ag doping. As revealed by the X-ray crystal structure, the Ag dopants exclusively reside on the icosahedral M_{12} shell while the center retains gold. The electron paramagnetic resonance (EPR) analysis indicates a clear shift in the *g*-values observed for the Ag-doped NCs in comparison to homogold $[Au_{25}(PET)_{18}]^0$ (2-phenylethanethiol (PET) = SC_2H_4Ph). The decrease in axial splitting in the *g*-tensor is attributed to the 4-time lower spin−orbit coupling of the Ag dopant than that of gold. A series of 7e M_{25} protected by the same ligand (PET) further demonstrates a linear shift in axial splitting with increasing amounts of Ag doping. The electronic structures of these NCs have been studied by time-dependent density functional theory (TDDFT) to provide insight into the depletion of electron density on Ag sites. We also report the preparation of a new NC $[Au_{25-x}Ag_x(o\text{-EBT})_{18}]^0$ (*o*-EBT = 2-ethylbenzenethiolate, av x = 5.8). Since the *o*-EBT ligand is the aromatic homologue of PET, the effect of ligand systems on axial splitting in comparable Ag-doped systems has been studied as well. The insight from NCs regarding the effects of spin−orbit coupling on magnetism could be expanded to larger (and less well defined) systems.

EXPERIMENTAL SECTION

Materials. Gold(III) chloride trihydrate ($HAuCl_4{\cdot}3H_2O$, 99.9% trace metal basis, Aldrich), silver nitrate ($AgNO_3$, >99.0%, Aldrich), tetraoctylammonium bromide (TOABr, >98%, Alfa Aesar), sodium borohydride ($NaBH_4$, >98%, Aldrich), 2-ethylbenzenethiol (*o*-EBT, >95%, Aldrich), 2-methylbenzenthiol (*o*-MBT, >98%, Alfa Aesar), 2-phenylethanethiol (PET, 99%, Aldrich), tetrahydrofuran (THF), methanol, dichloromethane (CH_2Cl_2), acetonitrile, and *n*-hexane (high performance liquid chromatography (HPLC) grade for all solvents) were used as received.

Synthesis. The $[Au_{25-x}Ag_x(o\text{-EBT})_{18}]^-$ (x = 4−7, counterion: Na^+) NC was synthesized by the following method: 8.62 mg of $AgNO_3$, 80 mg of $HAuCl_4{\cdot}3H_2O$ (Ag/Au molar ratio = 1:4), and 82 μL of *o*-EBT were mixed in THF, and then co-reduced with aqueous solution of $NaBH_4$ (144 mg). After 1 h of reaction, the product was washed with methanol once, and in the second time, $[Au_{25-x}Ag_x(o\text{-EBT})_{18}]^-$ was extracted into methanol (see the Supporting Information (SI) for more details). The obtained anionic NCs were then dissolved in dichloromethane and mixed with silica gel (pore size 60 Å, ∼300 mesh) for 15 min. The stripping of the counterion by silica gel leads to facile oxidation of $[Au_{25-x}Ag_x(o\text{-EBT})_{18}]^-$ to neutral $[Au_{25-x}Ag_x(o\text{-EBT})_{18}]^0$ by O_2. Crystallization of $[Au_{25-x}Ag_x(o\text{-EBT})_{18}]^0$ was performed by layer diffusion of hexane into a CH_2Cl_2 solution of the NCs within 2 days. $[Au_{25-x}Ag_x(o\text{-MBT})_{18}]^-$ (x = 4−7) NC was synthesized in the same way except the *o*-EBT ligands were replaced by *o*-MBT.

To prepare a series of $[Au_{25-x}Ag_x(PET)_{18}]^-$ NCs with different ranges of x, various amount of $AgNO_3$ vs 80 mg $HAuCl_4{\cdot}3H_2O$ (different Ag/Au molar ratios of 0:100; 1:100; 1:35; 1:8; or 1:4, see Table S1) were mixed with 130 mg TOABr, 150 μL PET in THF and stirred for 30 min. Then, an aqueous solution of $NaBH_4$ (77 mg) was added. After reacting overnight, the crude product was washed with methanol twice and then extracted into acetonitrile. The oxidation process was the same as $[Au_{25-x}Ag_x(o\text{-EBT})_{18}]^-$.

Characterization. UV−vis spectra of the NCs were measured on a Hewlett-Packard Agilent 8453 diode array spectrophotometer at room temperature. Matrix-assisted laser desorption/ionization mass spectrometry (MALDI-MS) was performed on a PerSeptive Biosystems Voyager DE super-STR time-of-flight (TOF) mass spectrometer. Electrospray ionization (ESI) MS was recorded using a Waters Q-TOF mass spectrometer equipped with Z-Spray Source. Single crystal X-ray diffraction data of $Au_{19.2}Ag_{5.8}(o\text{-EBT})_{18}$ were collected on a Bruker X8 Prospector Ultra equipped with an Apex II CCD detector and an IμS microfocus Cu Kα X-ray source (λ = 1.54178 Å). A piece of dark red block crystal with dimensions 0.08 × 0.04 × 0.02 mm^3 was mounted onto a MiTeGen MicroMount. Data collection was performed at 230 K.

The $[Au_{25-x}Ag_x(SR)_{18}]^0$ frozen solutions were used for EPR measurements. X-band EPR spectra were recorded on a Bruker ELEXSYS spectrometer equipped with an Oxford ESR-910 liquid helium cryostat and a Bruker bimodal cavity for the generation of microwave fields parallel and transverse to the applied magnetic field. The quantification of all signals was performed relative to a Cu EDTA spin standard prepared from a copper atomic absorption standard (Sigma-Aldrich). The microwave frequency was calibrated with a frequency counter, and the magnetic field was measured with an NMR gaussmeter. The sample temperature was calibrated against a calibrated Cernox sensor (Lakeshore CX-1050) mounted inside an EPR tube. A modulation frequency of 100 kHz was used for all EPR spectra.

RESULTS AND DISCUSSION

Characterization of $[Au_{25-x}Ag_x(SR)_{18}]^q$. The UV−vis absorption, MALDI-MS, and ESI-MS analyses of the $[Au_{25-x}Ag_x(o\text{-EBT})_{18}]^q$ NCs are given in Figures S1 and S2.

After the one-electron oxidation, the two charge states of $[Au_{25-x}Ag_x(o\text{-EBT})_{18}]^q$ (q = −1, 0) show prominent changes in optical spectra, and the optical gap decreases from 1.30 eV for the anion to 1.22 eV for the neutral (Figure 1a). The absorption

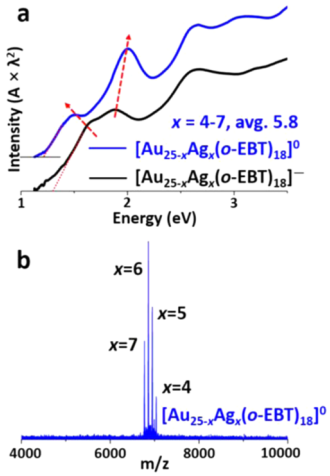

Figure 1. (a) UV−vis absorption spectra (on energy scale) of $[Au_{25-x}Ag_x(o\text{-EBT})_{18}]^q$ (q = −1 (black) and 0 (blue)); (b) ESI-MS spectrum of $[Au_{25-x}Ag_x(o\text{-EBT})_{18}]^0$.

peaks at the low-energy region diverge after oxidation (see red arrows, Figure 1a), which can be explained by TDDFT that the HOMO-1 and HOMO-2 levels of the neutral $[Au_{19}Ag_6(o\text{-EBT})_{18}]^0$ are much more separated from the HOMO than in the anionic $[Au_{19}Ag_6(o\text{-EBT})_{18}]^-$ (Figure S3). The absorption peak at the lowest energy (1.5 eV) of $[Au_{19}Ag_6(o\text{-EBT})_{18}]^0$ due to the Jahn−Teller-like distortion[26] is too weak to be observed in the 7e homogold $[Au_{25}(PET)_{18}]^0$ (PET = SC_2H_4Ph, Figure S4).[27,28] The ESI-MS spectrum shows peaks for x = 4−7 (Figure 1b), a similar range of x values to those in the literature.[29] Replacing *o*-EBT with *o*-MBT gave almost identical results in absorption spectra (Figure S5a) and MS spectra (except mass shift due to the *o*-EBT/*o*-MBT difference) (Figures S5b and S6 for MALDI and ESI, respectively).

As revealed by the crystal structure of $[Au_{25-x}Ag_x(o\text{-EBT})_{18}]^0$ (av x = 5.8, Figure 2a, Table S2), all Ag dopants are located on the icosahedral M_{12} shell. The average number of Ag dopants (x = 5.8) according to the crystal data is consistent with the ESI-MS result (x = 6 being the most abundant, Figure 1b). The ligand

https://dx.doi.org/10.1021/acs.chemmater.0c02984
Chem. Mater. 2020, 32, 9238−9244

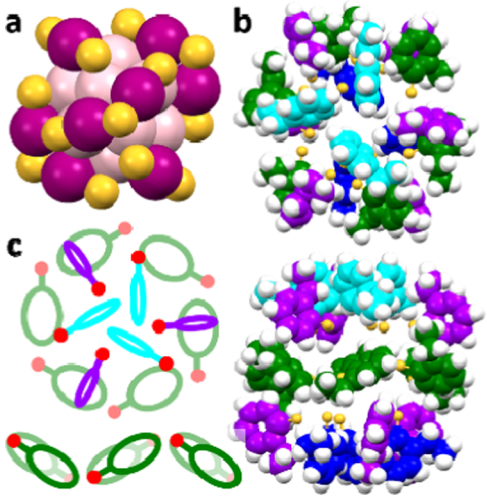

Figure 2. (a) Crystal structure and (b) top and side views of the ligand shell of $[Au_{25-x}Ag_x(o\text{-EBT})_{18}]^0$ (av x = 5.8). (c) *o*-EBT ligand arrangement in the ligand shell. Color labels: magenta = Au, pink = Au/Ag, yellow = S, cyan/purple/green = C, and white = H.

shell of $[Au_{25-x}Ag_x(o\text{-EBT})_{18}]^0$ differs from that of $[Au_{25}(SR)_{18}]^0$ by exhibiting spiral patterns along the C_3 axis of the cluster on the top and at the bottom, respectively (Figure 2b,c, marked in cyan and purple), as well as a chair-shaped pattern surrounding the waist (Figure 2b,c, marked in green).

We attempted to dope different amounts of Ag into $M_{25}(o\text{-EBT})_{18}$. However, irrespective of the Ag/Au molar ratio in the precursor, the *o*-EBT-protected M_{25} system predominantly funneled to an average Ag number of ~6. This funneling behavior can be explained by theoretical analysis (shown in Figure S7), and Ag doping up to 6 dopants falls very close to the parity between the shell-to-core binding energy and the core cohesive energy, more favorable than the monodoping of Ag. At 10 dopants or greater, the M_{25} NCs deviate significantly from the 95% confidence interval. Indicating a relative measure of instability (based on the Thermodynamic Stability Model, the core cohesive energy and shell-to-core binding energy of the NCs should be balanced).[30,31] Thus, the funneling to $x \sim 6$ in the *o*-EBT (or *o*-MBT)-protected M_{25} system is primarily due to thermodynamics, although the spread in the number of doped Ag atoms can still be observed in mass spectra. This ligand-dependent doping behavior captured by the above calculations is interesting and worth further experimental exploration in future research.

Given the inability to tune the *o*-EBT-protected M_{25} system, we sought to the PET-protected M_{25}, in which the different Ag doping ranges are synthetically accessible for $x < 12$.[32] Specifically, a series of $[Au_{25-x}Ag_x(PET)_{18}]^-$ were first synthesized (Figure S8) by controlling the Ag/Au molar ratios in the precursor (different amounts of $HAuCl_4{\cdot}3H_2O$ vs $AgNO_3$, Table S1), followed by silica gel-assisted oxidation to produce the corresponding $[M_{25}(PET)_{18}]^0$ (Figures 3 and S9), see the Supporting Information (SI) for details. The optical absorption spectra of M_{25} (q = −1, 0) are sensitive to Ag doping and continuously vary with the incorporation of more Ag atoms (Figures S8 and 3a). No detectable change was found in the MALDI-MS spectra (both positive and negative modes) for the same sample before and after oxidation (Figures S8c and 3b). The detailed MS spectra of the neutral $[Au_{25-x}Ag_x(PET)_{18}]^0$ series are shown in Figure 3b, including sample A: x = 0; sample

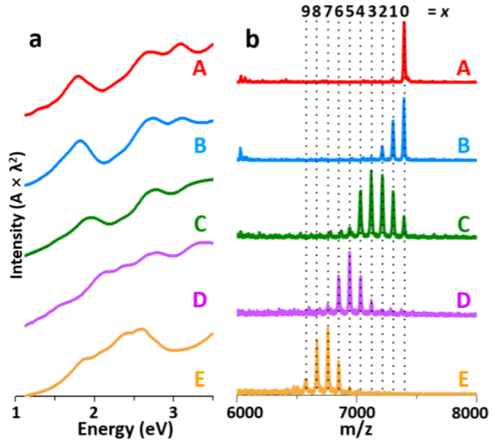

Figure 3. (a) UV−vis absorption spectra (on energy scale) and (b) MALDI-MS spectra of $[Au_{25-x}Ag_x(PET)_{18}]^-$.

B: x = 0−2 (av 0.58); sample C: x = 0−6 (av 2.39); sample D: x = 3−7 (av 4.89); and sample E: x = 5−9 (av 7.23), calculated based on the relative populations determined by MALDI-MS spectra.

Spin Properties. To measure the EPR spectra, $[Au_{25-x}Ag_x(PET)_{18}]^0$ crystals were dissolved in dry chloroform, which formed clear glass at cryogenic temperatures. Figure 4

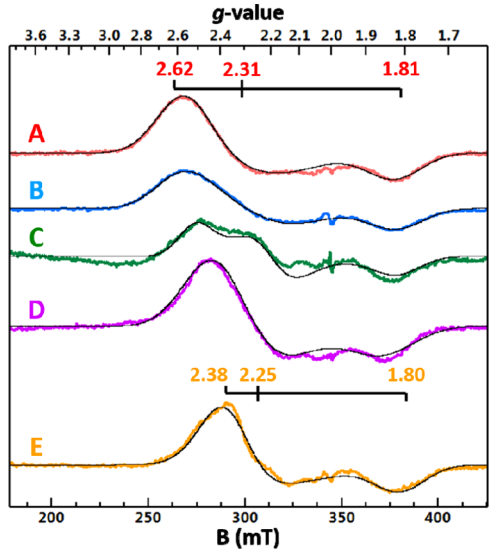

Figure 4. X-band (9.645 GHz) EPR spectra of $[Au_{25-x}Ag_x(PET)_{18}]^0$ with x ranging from 0 to 9 at 16 K. Microwave power 0.2 mW. The Ag dopant x is (A) 0, (B) 0−2, (C) 0−6, (D) 3−7, and (E) 5−9.

shows the X-band (9.645 GHz) EPR spectra of $[Au_{25-x}Ag_x(PET)_{18}]^0$ (x = 0−9) recorded at a temperature of 16 K. The g-tensors of the various species are determined from the simulations overlaid on the data. The spectrum of $[Au_{25}(PET)_{18}]^0$ (sample A) is consistent with that in our previous report.[18] However, the g-values (S = 1/2 signal, g = (2.62, 2.31, and 1.81)) are slightly different because the simulations do not include a hyperfine term. Note that if the hyperfine term is considered for $[Au_{25}(PET)_{18}]^0$, the g-values are (2.56, 2.32, and 1.87). EPR quantification indicates the presence of one unpaired spin per particle. To further understand the role of Ag heteroatoms in effecting the EPR signal of the NCs, we have studied a series of

https://dx.doi.org/10.1021/acs.chemmater.0c02984
Chem. Mater. 2020, 32, 9238−9244

$[Au_{25-x}Ag_x(PET)_{18}]^0$ (x = 1 to 9) NCs. We observe a gradual decrease in the g_x and g_y values with an increase in doping. As noted in Figure 4, sample E, these values decrease to 2.38 and 2.25 for $[Au_{25-x}Ag_x(PET)_{18}]^0$ (x = 5−9, av 7.23) in comparison to those for $[Au_{25}(PET)_{18}]^0$. The g-values of other samples are listed in Table S3. Anisotropy in the g-tensor is attributed to the spin−orbit coupling of the unpaired electron delocalized over the metal atoms in bonding. The spin−orbit coupling parameter of Au (~14 400 cm^{-1}) is almost 4-fold greater than that of Ag (~3470 cm^{-1}),[33] thus giving us a basis to understand our observations of decreased splitting in the g-values with Ag doping. Furthermore, these changes indicate that the electron delocalization extends over the dopant sites in the M_{25} system.

Since the doped samples (B−E) are mixtures of multiple species, e.g., sample B is a mixture of Au_{25}, $Au_{24}Ag_1$, and $Au_{23}Ag_2$ NCs, the observed EPR signals are broadened, especially for sample C, where x ranges from 0 to 6. However, the simulations are in good correlation with the MS data. With regard to the isolation of alloy NCs, Negishi et al. recently developed an impressive four-step method to separate $Au_{25-x}Ag_x(SC_4H_9)_{18}$ according to the x value,[34] which would be helpful in obtaining narrower EPR signals, but this is nevertheless challenging and has to be deferred to future work. Since the XRD structure reveals that the center and exterior staple motifs exclusively containing Au,[29] the broadening in signal is caused by the distribution of 'x' in the $Au_{12-x}Ag_x$ shell. Thus, the decrease in axial splitting can be directly linked to the increase in the average Ag doping number (0, 0.58, 2.39, 4.89, and 7.23 for samples A, B, C, D, and E, respectively, Figure 5). The linear trend gives rise to g_x = 2.25 at the maximum x of 12 (i.e., all of the icosahedral shell sites become Ag atoms).

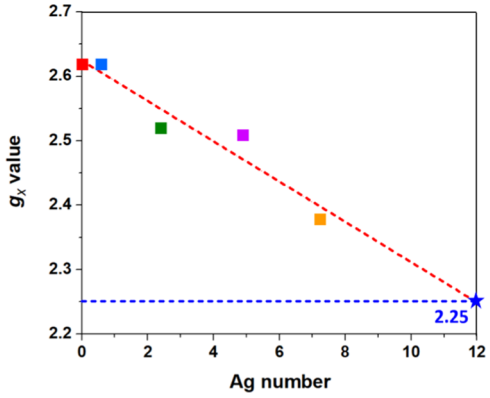

Figure 5. Plot of g_x vs the average Ag doping number in $Au_{25-x}Ag_x$ (or the $Au_{12-x}Ag_x$ shell since the center and exterior staple motifs contain gold exclusively) with maximum x being 12 and the corresponding fit.

The 7e nature of $[Au_{25-x}Ag_x(o\text{-EBT})_{18}]^0$ protected by aromatic ligand was also probed by low-temperature (16 K) EPR spectroscopy. The cluster was dissolved in dry chloroform, and the frozen sample (glass state) shows an S = 1/2 signal with g = (2.34, 2.20, and 1.84) (Figure 6, blue line). Decreasing the amplitude of the magnetic modulation has no effect on the line shape, and there is no evidence of resolved hyperfine splitting from the ^{197}Au nuclei (I = 3/2, natural abundance 100%). Overall, the reduced axial splitting upon Ag doping in $[Au_{25-x}Ag_x(o\text{-EBT})_{18}]^0$ is consistent with the case of $[Au_{25-x}Ag_x(PET)_{18}]^0$ series. We note that our oxidation process is too gentle to obtain the deeply oxidized 6e $[M_{25}(SR)_{18}]^+$, but

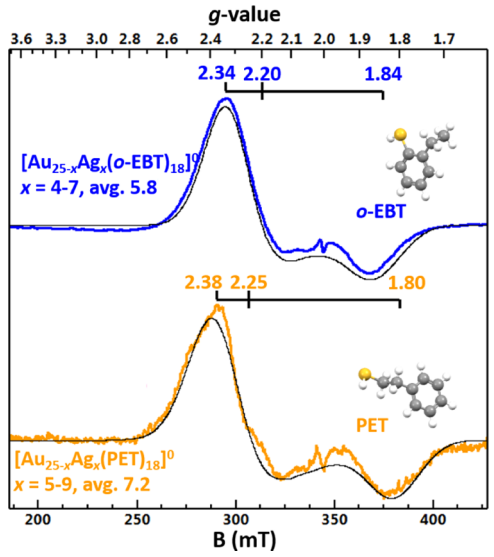

Figure 6. Comparison of the X-band EPR spectra of $[Au_{25-x}Ag_x(o\text{-EBT})_{18}]^0$ (x = 4−7, av 5.8) with g = (2.34, 2.25, and 1.84) and $[Au_{25-x}Ag_x(PET)_{18}]^0$ (x = 5−9, av 7.2) with g = (2.38, 2.25, and 1.80) at 16 K and a microwave power of 0.2 mW. The ligand structures are shown aside.

the latter would be diamagnetic as the case of $[Au_{25}(SR)_{18}]^+$ with no EPR signal.[35]

The Ag doping in the M_{12} shell for both $[Au_{25-x}Ag_x(o\text{-EBT})_{18}]^0$ and the $[Au_{25-x}Ag_x(PET)_{18}]^0$ series indicates that the spin is primarily delocalized on M_{12} since the twelve sites are equivalent. Note that the effect of the central atom on EPR cannot be fully excluded, as Ag cannot be doped into the center of M_{25}. Very recently, the Tsukuda group[36] reported the 7e $[Pt@Au_{24}(PET)_{18}]^-$ and its EPR (of a frozen solution) with an orthorhombic g = (2.57, 2.37, and 1.75), being almost the same as its homogold counterpart,[18] suggesting comparable contributions of spin densities to the 1P superatomic orbital from the central Pt atom in the $[PtAu_{12}]^{5+}$ kernel and the central Au in the $[Au_{13}]^{6+}$ kernel. We rationalize that although Pt is center-accessible, the spin−orbit coupling parameter of Pt is very close to that of Au,[33] and thus, no shift for 7e $[Pt@Au_{24}(PET)_{18}]^-$ compared to $[Au_{25}(PET)_{18}]^0$.

Moreover, when comparing the magnetic properties between $[Au_{25-x}Ag_x(o\text{-EBT})_{18}]^0$ (x = 4−7, av 5.8) and $[Au_{25-x}Ag_x(PET)_{18}]^0$ (x = 5−9, av 7.2; Figure 6, yellow line), which have comparable Ag doping ranges, we notice that the protecting ligands could have some minor influence on splitting in the g-values (Figure 6). Literature reports show the effect of the ligand on the g-factor of the metallic-state electrons.[37] Note that the two thiolates (o-EBT and PET) are isomers with the same formula of SC_8H_9, facilitating the study of the aromatic vs nonaromatic ligand effect. The results show a subtle decrease in axial splitting in $[Au_{25-x}Ag_x(o\text{-EBT})_{18}]^0$ (x = av 5.8, g_x = 2.34) in comparison to $[Au_{25-x}Ag_x(PET)_{18}]^0$ (x = av 7.2, g_x = 2.38), see Table S3. This effect is in contrast to the doping trend, i.e., less Ag-doped $[Au_{25-x}Ag_x(o\text{-EBT})_{18}]^0$ shows a greater reduction in axial splitting than the nonaromatic-ligand capped-$[Au_{25-x}Ag_x(PET)_{18}]^0$. This result makes us consider other possible factors that may contribute to axial splitting: (1) the electronic structure of the NC might be influenced differently by aromatic and nonaromatic ligand systems;[38] (2) the interactions between the metal kernel and the capping ligands might also play some role in magnetism.[39]

https://dx.doi.org/10.1021/acs.chemmater.0c02984
Chem. Mater. 2020, 32, 9238−9244

TDDFT Calculation. The atomic charges of $[Au_{19}Ag_6(SR)_{18}]^0$ have been studied by Bader charge analysis, with $[Au_{25}(PET)_{18}]^0$ as the reference (Table 1). The charges of the icosahedral Au_6Ag_6 shells in $[Au_{19}Ag_6(o\text{-EBT})_{18}]^0$ and $[Au_{19}Ag_6(PET)_{18}]^0$ are ∼+1.50e and ∼+1.44e, respectively, while that of the Au_{12} shell in $[Au_{25}(PET)_{18}]^0$ is only ∼+0.60e. This indicates that the valence electrons are more depleted in the M_{12} shell for Ag-doped M_{25} NCs due to the large difference of electronegativity (χ) between Ag (χ = 1.93) and S (χ = 2.58), while the difference between Au (χ = 2.54) and S is very small (hence, less charge transfer). The charge depletion due to Ag doping also relates to the change in spin density, which is reflected in the change of EPR spectra. As to the two Ag-doped NCs capped by different ligands (aromatic vs nonaromatic), the largest difference lies in the S atoms of $[Au_{19}Ag_6(PET)_{18}]^0$, which holds a more negative charge (−0.882e/cluster higher) than $[Au_{19}Ag_6(o\text{-EBT})_{18}]^0$. The electron redistribution may have minor contributions to this slight difference in magnetism for the two NCs capped by different ligands.

Table 1. Bader Charge Analysis for $[Au_{19}Ag_6(o\text{-EBT})_{18}]^0$, $[Au_{19}Ag_6(PET)_{18}]^0$, and $[Au_{25}(PET)_{18}]^0$ NCs per Atom Type, Respectively[a]

	$[Au_{19}Ag_6(o\text{-EBT})_{18}]^0$	$[Au_{19}Ag_6(PET)_{18}]^0$	$[Au_{25}(PET)_{18}]^0$
Au_{center}	−0.182	−0.205	−0.075
Au_{shell}	−0.028	−0.012	0.050
Ag_{shell}	0.278	0.252	
Au_{motifs}	0.109	0.081	0.096
S	−0.129	−0.178	−0.154
C	−0.060	−0.057	−0.059
H	0.051	0.057	0.059

[a]The charges are calculated (and averaged) for Au_{center}, 6 Au_{shell}, and 6 Ag_{shell} of $Au_{19}Ag_6$ or 12 Au_{shell} of Au_{25}, 12 Au_{motifs} and 18 S atoms in the staple motifs and 144 C and 162 H atoms in the organic layer.

The electronic structure and optical transitions of $[Au_{19}Ag_6(SR)_{18}]^0$ with different −R groups as well as their corresponding Kohn−Sham (KS) energy diagrams are further compared (Figure S10, Table S4). In the simulated spectrum of $[Au_{19}Ag_6(o\text{-EBT})_{18}]^0$, the absorption peaks below 1.0 eV (Figure S10b, peak (i)) arise from the electronic transitions from the fully occupied molecular orbitals to the partially occupied molecular orbital (i.e., HOMO) and the lowest unoccupied molecular orbital (LUMO) and LUMO + 1 orbitals are almost degenerated (Figure S10c). By contrast, in $[Au_{19}Ag_6(PET)_{18}]^0$, the LUMO/LUMO + 1 states are distinctively separated, forming two peaks (i/ii), and the HOMO−LUMO transition (peak i) is too weak to be detected experimentally (Figure S10d−f). In addition, the HOMO of $[Au_{19}Ag_6(PET)_{18}]^0$ is located much higher than HOMO-1/-2 levels compared to those states of $[Au_{19}Ag_6(o\text{-EBT})_{18}]^0$ (Figure S10c,f).

CONCLUSIONS

In summary, this work presents the results on manipulating the paramagnetism of the 7e $[M_{25}(SR)_{18}]^0$ (M = Au/Ag) NCs by Ag doping. A clear shift of g-values for $[Au_{25-x}Ag_x(o\text{-EBT})_{18}]^0$ is observed compared to homogold $[Au_{25}(PET)_{18}]^0$. A series of $[M_{25}(PET)_{18}]^0$ NCs further demonstrates a gradual and linear shift in g_x with increasing Ag dopants in the M_{12} shell. The reduced axial splitting upon Ag doping is explained by the large difference in spin−orbit coupling of the two metal atoms. The doping Ag atoms, which are related to the spin, are only found on the M_{12} shell. In addition, the influence of aromatic and nonaromatic ligands on the orbitals and electronic excitations of the NCs is also studied by TDDFT calculations. Overall, this work provides insight into the paramagnetism in the 7e $[M_{25}(SR)_{18}]^0$ and offers a strategy for tailoring the magnetic properties of atomically precise NCs via doping.

ASSOCIATED CONTENT

Supporting Information

The Supporting Information is available free of charge at https://pubs.acs.org/doi/10.1021/acs.chemmater.0c02984.

Details of syntheses, characterization, and measurements (PDF)

X-ray crystallographic data for $[Au_{25-x}Ag_x(o\text{-EBT})_{18}]^0$ (x = 4−7) (CIF)

AUTHOR INFORMATION

Corresponding Authors

Michael P. Hendrich − *Department of Chemistry, Carnegie Mellon University, Pittsburgh, Pennsylvania 15213, United States;* orcid.org/0000-0003-4775-0389; Email: hendrich@andrew.cmu.edu

Rongchao Jin − *Department of Chemistry, Carnegie Mellon University, Pittsburgh, Pennsylvania 15213, United States;* orcid.org/0000-0002-2525-8345; Email: rongchao@andrew.cmu.edu

Authors

Yingwei Li − *Department of Chemistry, Carnegie Mellon University, Pittsburgh, Pennsylvania 15213, United States;* orcid.org/0000-0002-4813-6009

Saborni Biswas − *Department of Chemistry, Carnegie Mellon University, Pittsburgh, Pennsylvania 15213, United States*

Tian-Yi Luo − *Department of Chemistry, University of Pittsburgh, Pittsburgh, Pennsylvania 15260, United States;* orcid.org/0000-0002-9973-9328

Rosalba Juarez-Mosqueda − *Department of Chemical Engineering, University of Pittsburgh, Pittsburgh, Pennsylvania 15261, United States*

Michael G. Taylor − *Department of Chemical Engineering, University of Pittsburgh, Pittsburgh, Pennsylvania 15261, United States*

Giannis Mpourmpakis − *Department of Chemical Engineering, University of Pittsburgh, Pittsburgh, Pennsylvania 15261, United States;* orcid.org/0000-0002-3063-0607

Nathaniel L. Rosi − *Department of Chemistry, University of Pittsburgh, Pittsburgh, Pennsylvania 15260, United States;* orcid.org/0000-0001-8025-8906

Complete contact information is available at: https://pubs.acs.org/10.1021/acs.chemmater.0c02984

Author Contributions

‖

Y.L. and S.B.contributed equally.

Funding

This work was funded by the National Science Foundation under grant NSF DMR-1808675 (R.J.), the National Institutes of Health under grant RO1 GM077387 (M.P.H.), and the NSF CBET-CAREER 1652694 (G.M.).

Notes

The authors declare no competing financial interest.

■ ACKNOWLEDGMENTS

Computational support was provided by the University of Pittsburgh Center for Research Computing and the Extreme Science and Engineering Discovery Environment supported by the NSF (ACI-1548562).

■ REFERENCES

(1) Zhang, P.; Sham, T. K. X-Ray Studies of the Structure and Electronic Behavior of Alkanethiolate-Capped Gold Nanoparticles: The Interplay of Size and Surface Effects. *Phys. Rev. Lett.* **2003**, *90*, No. 245502.
(2) Garitaonandia, J. S.; Insausti, M.; Goikolea, E.; Suzuki, M.; Cashion, J. D.; Kawamura, N.; Ohsawa, H.; Gil de Muro, I.; Suzuki, K.; Plazaola, F.; Rojo, T. Chemically Induced Permanent Magnetism in Au, Ag, and Cu Nanoparticles: Localization of the Magnetism by Element Selective Techniques. *Nano Lett.* **2008**, *8*, 661−667.
(3) de la Venta, J.; Pucci, A.; Fernández Pinel, E.; García, M. A.; de Julián Fernandez, C.; Crespo, P.; Mazzoldi, P.; Ruggeri, G.; Hernando, A. Magnetism in Polymers with Embedded Gold Nanoparticles. *Adv. Mater.* **2007**, *19*, 875−877.
(4) Dutta, P.; Pal, S.; Seehra, M. S.; Anand, M.; Roberts, C. B. Magnetism in Dodecanethiol-Capped Gold Nanoparticles: Role of Size and Capping Agent. *Appl. Phys. Lett.* **2007**, *90*, No. 213102.
(5) Guerrero, E.; Muñoz-Márquez, M. A.; García, M. A.; Crespo, P.; Fernández-Pinel, E.; Hernando, A.; Fernández, A. Surface Plasmon Resonance and Magnetism of Thiol-Capped Gold Nanoparticles. *Nanotechnology* **2008**, *19*, No. 175701.
(6) Kumar, C. S. S. R.; Mohammad, F. Magnetic Gold Nanoshells: Stepwise Changing of Magnetism through Stepwise Biofunctionalization. *J. Phys. Chem. Lett.* **2010**, *1*, 3141−3146.
(7) Nealon, G. L.; Donnio, B.; Greget, R.; Kappler, J.-P.; Terazzi, E.; Gallani, J.-L. Magnetism in Gold Nanoparticles. *Nanoscale* **2012**, *4*, 5244−5258.
(8) Hori, H.; Yamamoto, Y.; Iwamoto, T.; Miura, T.; Teranishi, T.; Miyake, M. Diameter Dependence of Ferromagnetic Spin Moment in Au Nanocrystals. *Phys. Rev. B* **2004**, *69*, No. 174411.
(9) Gréget, R.; Nealon, G. L.; Vileno, B.; Turek, P.; Mény, C.; Ott, F.; Derory, A.; Voirin, E.; Rivière, E.; Rogalev, A.; Wilhelm, F.; Joly, L.; Knafo, W.; Ballon, G.; Terazzi, E.; Kappler, J.-P.; Donnio, B.; Gallani, J.-L. Magnetic Properties of Gold Nanoparticles: A Room-Temperature Quantum Effect. *ChemPhysChem* **2012**, *13*, 3092−3097.
(10) Crespo, P.; Litrán, R.; Rojas, T. C.; Multigner, M.; de la Fuente, J. M.; Sánchez-López, J. C.; García, M. A.; Hernando, A.; Penadés, S.; Fernández, A. Permanent Magnetism, Magnetic Anisotropy, and Hysteresis of Thiol-Capped Gold Nanoparticles. *Phys. Rev. Lett.* **2004**, *93*, No. 087204.
(11) Trudel, S. Unexpected Magnetism in Gold Nanostructures: Making Gold Even More Attractive. *Gold Bull.* **2011**, *44*, 3−13.
(12) Singh, R. Unexpected Magnetism in Nanomaterials. *J. Magn. Magn. Mater.* **2013**, *346*, 58−73.
(13) Hembury, M.; Chiappini, C.; Bertazzo, S.; Kalber, T. L.; Drisko, G. L.; Ogunlade, O.; Walker-Samuel, S.; Krishna, K. S.; Jumeaux, C.; Beard, P.; Kumar, C. S. S. R.; Porter, A. E.; Lythgoe, M. F.; Boissière, C.; Sanchez, C.; Stevens, M. M. Gold−Silica Quantum Rattles for Multimodal Imaging and Therapy. *Proc. Natl. Acad. Sci. U.S.A.* **2015**, *112*, 1959−1964.
(14) Jin, R. Atomically Precise Metal Nanoclusters: Stable Sizes and Optical Properties. *Nanoscale* **2015**, *7*, 1549−1565.
(15) Jin, R.; Zeng, C.; Zhou, M.; Chen, Y. Atomically Precise Colloidal Metal Nanoclusters and Nanoparticles: Fundamentals and Opportunities. *Chem. Rev.* **2016**, *116*, 10346−10413.
(16) Li, Y.; Higaki, T.; Du, X.; Jin, R. Chirality and Surface Bonding Correlation in Atomically Precise Metal Nanoclusters. *Adv. Mater.* **2020**, No. 1905488.
(17) Roduner, E.; Jensen, C. Magnetic Properties and the Superatom Character of 13-Atom Platinum Nanoclusters. *Magnetochemistry* **2015**, *1*, 28−44.
(18) Zhu, M.; Aikens, C. M.; Hendrich, M. P.; Gupta, R.; Qian, H.; Schatz, G. C.; Jin, R. Reversible Switching of Magnetism in Thiolate-Protected Au_{25} Superatoms. *J. Am. Chem. Soc.* **2009**, *131*, 2490−2492.
(19) Song, Y.; Jin, S.; Kang, X.; Xiang, J.; Deng, H.; Yu, H.; Zhu, M. How a Single Electron Affects the Properties of the "Non-Superatom" Au_{25} Nanoclusters. *Chem. Mater.* **2016**, *28*, 2609−2617.
(20) Liu, X.; Chen, J.; Yuan, J.; Li, Y.; Li, J.; Zhou, S.; Yao, C.; Liao, L.; Zhuang, S.; Zhao, Y.; Deng, H.; Yang, J.; Wu, Z. A Silver Nanocluster Containing Interstitial Sulfur and Unprecedented Chemical Bonds. *Angew. Chem.* **2018**, *130*, 11443−11447.
(21) Zeng, C.; Weitz, A.; Withers, G.; Higaki, T.; Zhao, S.; Chen, Y.; Gil, R. R.; Hendrich, M.; Jin, R. Controlling Magnetism of $Au_{133}(TBBT)_{52}$ Nanoclusters at Single Electron Level and Implication for Nonmetal to Metal Transition. *Chem. Sci.* **2019**, *10*, 9684−9691.
(22) Herbert, P. J.; Window, P.; Ackerson, C. J.; Knappenberger, K. L. Low-Temperature Magnetism in Nanoscale Gold Revealed through Variable-Temperature Magnetic Circular Dichroism Spectroscopy. *J. Phys. Chem. Lett.* **2019**, *10*, 189−193.
(23) Hirai, H.; Takano, S.; Nakamura, T.; Tsukuda, T. Understanding Doping Effects on Electronic Structures of Gold Superatoms: A Case Study of Diphosphine-Protected $M@Au_{12}$ (M = Au, Pt, Ir). *Inorg. Chem.* **2020**, DOI: 10.1021/acs.inorgchem.0c00879.
(24) Venzo, A.; Antonello, S.; Gascón, J. A.; Guryanov, I.; Leapman, R. D.; Perera, N. V.; Sousa, A.; Zamuner, M.; Zanella, A.; Maran, F. Effect of the Charge State (z = 1, 0, +1) on the Nuclear Magnetic Resonance of Monodisperse $Au_{25}[S(CH_2)_2Ph]_{18}^{z}$ Clusters. *Anal. Chem.* **2011**, *83*, 6355−6362.
(25) Chauhan, V.; Sahoo, S.; Khanna, S. N. $Ni_9Te_6(PEt_3)_8C_{60}$ Is a Superatomic Superalkali Superparamagnetic Cluster Assembled Material (S^3-CAM). *J. Am. Chem. Soc.* **2016**, *138*, 1916−1921.
(26) Kwak, K.; Tang, Q.; Kim, M.; Jiang, D.; Lee, D. Interconversion between Superatomic 6-Electron and 8-Electron Configurations of $M@Au_{24}(SR)_{18}$ Clusters (M = Pd, Pt). *J. Am. Chem. Soc.* **2015**, *137*, 10833−10840.
(27) Zhu, M.; Eckenhoff, W. T.; Pintauer, T.; Jin, R. Conversion of Anionic $[Au_{25}(SCH_2CH_2Ph)_{18}]^-$ Cluster to Charge Neutral Cluster via Air Oxidation. *J. Phys. Chem. C* **2008**, *112*, 14221−14224.
(28) Tofanelli, M. A.; Salorinne, K.; Ni, T. W.; Malola, S.; Newell, B.; Phillips, B.; Häkkinen, H.; Ackerson, C. J. Jahn-Teller Effects in $Au_{25}(SR)_{18}$. *Chem. Sci.* **2016**, *7*, 1882−1890.
(29) Kumara, C.; Aikens, C. M.; Dass, A. X-Ray Crystal Structure and Theoretical Analysis of $Au_{25-x}Ag_x(SCH_2CH_2Ph)_{18}^-$ Alloy. *J. Phys. Chem. Lett.* **2014**, *5*, 461−466.
(30) Taylor, M. G.; Mpourmpakis, G. Thermodynamic Stability of Ligand-Protected Metal Nanoclusters. *Nat. Commun.* **2017**, *8*, No. 15988.
(31) Taylor, M. G.; Mpourmpakis, G. Rethinking Heterometal Doping in Ligand-Protected Metal Nanoclusters. *J. Phys. Chem. Lett.* **2018**, *9*, 6773−6778.
(32) Negishi, Y.; Iwai, T.; Ide, M. Continuous Modulation of Electronic Structure of Stable Thiolate-Protected Au_{25} Cluster by Ag Doping. *Chem. Commun.* **2010**, *46*, 4713−4715.
(33) Martin, W. C. Table of Spin-Orbit Energies for *p*-Electrons in Neutral Atomic (Core)*np* Configurations. *J. Res. Natl. Bur. Stand., Sect. A* **1971**, *75A*, 109−111.
(34) Niihori, Y.; Koyama, Y.; Watanabe, S.; Hashimoto, S.; Hossain, S.; Nair, L. V.; Kumar, B.; Kurashige, W.; Negishi, Y. Atomic and Isomeric Separation of Thiolate-Protected Alloy Clusters. *J. Phys. Chem. Lett.* **2018**, *9*, 4930−4934.
(35) Antonello, S.; Perera, N. V.; Ruzzi, M.; Gascón, J. A.; Maran, F. Interplay of Charge State, Lability, and Magnetism in the Molecule-like $Au_{25}(SR)_{18}$ Cluster. *J. Am. Chem. Soc.* **2013**, *135*, 15585−15594.
(36) Suyama, M.; Takano, S.; Nakamura, T.; Tsukuda, T. Stoichiometric Formation of Open-Shell $[PtAu_{24}(SC_2H_4Ph)_{18}]^-$ via Spontaneous Electron Proportionation between $[PtAu_{24}(SC_2H_4Ph)_{18}]^{2-}$ and $[PtAu_{24}(SC_2H_4Ph)_{18}]^0$. *J. Am. Chem. Soc.* **2019**, *141*, 14048−14051.
(37) Cirri, A.; Silakov, A.; Jensen, L.; Lear, B. J. Chain Length and Solvent Control over the Electronic Properties of Alkanethiolate-

Protected Gold Nanoparticles at the Molecule-to-Metal Transition. *J. Am. Chem. Soc.* **2016**, *138*, 15987−15993.
(38) Li, Y.; Juarez-Mosqueda, R.; Song, Y.; Zhang, Y.; Chai, J.; Mpourmpakis, G.; Jin, R. Ligand Exchange on $Au_{38}(SR)_{24}$: Substituent Site Effects of Aromatic Thiols. *Nanoscale* **2020**, *12*, 9423−9429.
(39) Agrachev, M.; Antonello, S.; Dainese, T.; Gascón, J. A.; Pan, F.; Rissanen, K.; Ruzzi, M.; Venzo, A.; Zoleo, A.; Maran, F. A Magnetic Look into the Protecting Layer of Au_{25} Clusters. *Chem. Sci.* **2016**, *7*, 6910−6918.

https://dx.doi.org/10.1021/acs.chemmater.0c02984
Chem. Mater. 2020, 32, 9238−9244